



Low Water Outgassing from (24) Themis and (65) Cybele: 3.1 μm Near-IR Spectral Implications

L. O'Rourke¹, T. G. Müller², N. Biver³, D. Bockelée-Morvan³, S. Hasegawa⁴, I. Valtchanov⁵, M. Küppers¹, S. Fornasier^{3,6}, H. Campins⁷, H. Fujiwara⁸, D. Teyssier⁵, and T. Lim⁵

¹ European Space Astronomy Centre, European Space Agency, Urbanización Villafraanca del Castillo, Villanueva de la Cañada, E-28692 Madrid, Spain
lorourke@esa.int

² Max-Planck-Institut für extraterrestrische Physik, Giessenbachstrasse 1, D-85748 Garching, Germany

³ LESIA, Observatoire de Paris, Université PSL, CNRS, Université de Paris, Sorbonne Université, 5 place Jules Janssen, F-92195 Meudon, France

⁴ Institute of Space and Astronautical Science, Japan Aerospace Exploration Agency, 3-1-1 Yoshinodai, Chuo-ku, Sagami-hara, Kanagawa 252-5210, Japan

⁵ Telespazio Vega UK Ltd. for ESA/ESAC, Urbanización Villafraanca del Castillo, Villanueva de la Cañada, E-28692, Madrid, Spain

⁶ Institut Universitaire de France (IUF), 1 rue Descartes, F-75231 Paris Cedex 05, France

⁷ University of Central Florida, P.O. Box 162385, Orlando, FL 32816-2385, USA

⁸ Subaru Telescope, National Astronomical Observatory of Japan, 650 North A'ohoku Place, Hilo, HI 96720, USA

Received 2020 May 31; revised 2020 July 10; accepted 2020 July 13; published 2020 July 31

Abstract

Asteroids (24) Themis and (65) Cybele have an absorption feature at 3.1 μm reported to be directly linked to surface water ice. We searched for water vapor escaping from these asteroids with the Herschel Space Observatory Heterodyne Instrument for the Far Infrared. While no H_2O line emission was detected, we obtain sensitive 3σ water production rate upper limits of $Q(\text{H}_2\text{O}) < 4.1 \times 10^{26}$ molecules s^{-1} for Themis and $Q(\text{H}_2\text{O}) < 7.6 \times 10^{26}$ molecules s^{-1} for Cybele. Using a thermophysical model, we merge data from the Subaru/Cooled Mid-Infrared Camera and Spectrometer and the Herschel/Spectral and Photometric Imaging Receiver with the contents of a multi-observatory database to derive new radiometric properties for these two asteroids. For Themis, we find a thermal inertia $\Gamma = 20^{+25}_{-10}$ $\text{J m}^{-2} \text{s}^{-1/2} \text{K}^{-1}$, a diameter 192^{+10}_{-7} km, and a geometric V-band albedo $p_V = 0.07 \pm 0.01$. For Cybele, we obtain a thermal inertia $\Gamma = 25^{+28}_{-19}$ $\text{J m}^{-2} \text{s}^{-1/2} \text{K}^{-1}$, a diameter 282 ± 9 km, and an albedo $p_V = 0.042 \pm 0.005$. Using all inputs, we estimate that water ice intimately mixed with the asteroids' dark surface material would cover $< 0.0017\%$ (for Themis) and $< 0.0033\%$ (for Cybele) of their surfaces, while an areal mixture with very clean ice (Bond albedo 0.8 for Themis and 0.7 for Cybele) would cover $< 2.2\%$ (for Themis) and $< 1.5\%$ (for Cybele) of their surfaces. While surface (and subsurface) water ice may exist in small localized amounts on both asteroids, it is not the reason for the observed 3.1 μm absorption feature.

Unified Astronomy Thesaurus concepts: Asteroids (72); Main belt asteroids (2036); Main-belt comets (2131); Comets (280); Small solar system bodies (1469); Astronomy data modeling (1859)

1. Introduction

Observational and theoretical data suggest that solar system objects located in the main asteroid belt hold more water ice than originally thought. Indeed, the detection of water vapor on (1) Ceres (Küppers et al. 2014; Combe et al. 2016), asteroids that present cometary behavior (active asteroids; Hsieh & Jewitt 2006), and 3.1 μm absorption features in asteroid reflectance spectra (Campins et al. 2010; Licandro et al. 2011) have reinforced this line of thinking. Hydrated minerals (any mineral containing H_2O or OH) and water ice are known to have strong spectral absorptions in the $\sim 2.5\text{--}3.5$ μm wavelength range (Rivkin et al. 2002). Features at 0.7 and 2.7 μm are attributed to the presence of hydrated minerals and those at ~ 3.05 μm to water ice.

Takir & Emery (2012) examined the distribution and abundance of hydrated minerals on 28 outer main-belt asteroids and proposed four 3 μm spectral groups based on the absorption shapes observed: Ceres-like, Europa-like, rounded, and sharp. Of the four absorption shapes, only the rounded 3 μm band shape has been linked to the presence of water ice on the surface. Besides being observed on both Themis (Fornasier et al. 1999; Campins et al. 2010; Rivkin & Emery 2010) and 65 Cybele (Licandro et al. 2011), it has been found on numerous other asteroids, e.g., (76) Freia (Hargrove et al. 2012) and (361) Bononia (Usui et al. 2019),

correlating well with laboratory experiments suggesting (Rivkin & Emery 2010) that a fine coating of ice on pyroxene grains mixed with amorphous carbon was covering the entire surface of these asteroids.

Asteroid (24) Themis is the parent body of the Themis family of asteroids located at the edge of the main belt and consisting of about 5000 members (Nesvorný 2012), mostly belonging to primordial C and B type (Fornasier et al. 2016a). In addition, to the 3.1 μm feature, the asteroid also has an absorption feature at approximately 2.76 μm associated with hydrated minerals (Usui et al. 2019), with no feature at 0.7 μm . Asteroid (65) Cybele, a P-type asteroid, is the most prominent member of a primitive outer-edge main-belt asteroid population known as the Cybele asteroids. Although it has the 3.1 μm feature, the asteroid has no hydrated features at 0.7 or 2.76 μm (Usui et al. 2019).

Besides the search for hydration in asteroids with spectral features from hydroxyl-bearing minerals (Takir & Emery 2012; Usui et al. 2019) or oxidized iron in phyllosilicates (Fornasier et al. 2014), the detection of gaseous water vapor or its disassociation products provides a more direct way to identify the presence of water. Up to now, water vapor has not been detected on Themis or Cybele, although upper limits have been derived for each.

Optical spectra of the two asteroids were obtained (Jewitt & Guilbert-Lepoutre 2012) from the Keck I 10 m telescope to

Table 1
Observations and Observing Conditions for the Previously Unpublished Measurements Used in This Paper

Target	Observatory and Instrument	ObsID	Date/Time (UT)	rh (au)	Δ (au)	α (deg)
Themis	Herschel HIFI (556.936 GHz)	1342262585	2013 Jan 30 17:30:38	2.92	2.37	18.1
	Subaru COMICS (<i>N</i> -band 8.8 μm)	n/a	2003 Jun 20 06:46:30	2.87	2.64	20.7
	Subaru COMICS (<i>N</i> -band 11.7 μm)	n/a	2003 Jun 20 06:43:30	2.87	2.64	20.7
Cybele	Herschel HIFI (556.936 GHz)	134225765	2012 Dec 21 16:53:19	3.52	3.11	15.5
	Herschel SPIRE (large map; 250/350/500 μm)	134187509	2009 Dec 1 13:14:28	3.45	3.27	16.6
		134187511	2009 Dec 1 13:44:47	3.45	3.27	16.6
		134228344	2011 Sep 8 16:48:43	3.80	4.09	14.1
	Herschel SPIRE (small map; 250/350/500 μm)	134230779	2011 Oct 10 22:51:21	3.79	3.61	15.2
		134244177	2012 Apr 12 19:47:23	3.72	3.86	15.1
		134244840	2012 Apr 22 18:30:51	3.72	3.99	14.4
		134254082	2012 Oct 28 19:50:08	3.57	3.93	14.2
		134255059	2012 Nov 15 00:37:22	3.56	3.68	15.6
		134257368	2012 Dec 17 23:39:25	3.53	3.16	15.7

Note. Columns: target (the two asteroids), observatory and instruments used, ObsID (observation ID reference number), date and time in UT, rh (heliocentric distance), Δ (Earth to asteroid distance), α (phase angle).

search for outgassed CN, a photodissociation product of HCN. An average CN/H₂O ratio of 0.3% was applied (as done for comets) to these asteroids, and upper limits for the water production rate of $Q(\text{H}_2\text{O}) < 1.3 \times 10^{28}$ molecules s⁻¹ for Themis and $Q(\text{H}_2\text{O}) < 1.2 \times 10^{28}$ molecules s⁻¹ were derived. A global coverage of water ice was discarded by the authors with these upper limits constraining the ice coverage on the Earth-facing asteroids' surface to be less than 10% based upon the presence of "relatively clean" (unmixed) ice with a Bond albedo >0.3.

Radio and UV observational searches for OH emission around Themis were performed (Lovell et al. 2010) using the National Radio Astronomy Observatory 100 m Green Bank Telescope and the Lowell Observatory 1.1 m Hall Telescope. A 3 σ upper limit for $Q(\text{H}_2\text{O})$ of 1×10^{28} molecules s⁻¹ was obtained.

A more recent study (McKay et al. 2017) presented the result of a nondetection following a search for gaseous H₂O at optical wavelengths using the forbidden oxygen line at 6300.3 Å, in line with similar observations performed on comets (McKay et al. 2014, 2015). While no detection was made, an upper limit of $Q(\text{H}_2\text{O}) < 4.5 \times 10^{27}$ molecules s⁻¹ was provided for Themis, and conclusions equivalent to Jewitt & Gilbert-Lepoutre (2012) were reached regarding the localized nature and purity of the ice needed to match the upper limit obtained.

The Heterodyne Instrument for the Far Infrared (HIFI; de Graauw et al. 2010) on board the ESA Herschel Space Observatory (Pilbratt et al. 2010) has proven to be the most sensitive instrument ever built for directly observing water vapor on comets (Bockelée-Morvan et al. 2010), as well as in the asteroid belt. Indeed, it was through use of HIFI that H₂O gas was successfully detected around (1) Ceres (Küppers et al. 2014).

In Section 2 the observations of Cybele and Themis obtained by HIFI, as well as those from the Subaru/Cooled Mid-Infrared Camera and Spectrometer (COMIC) and Herschel/Spectral and Photometric Imaging Receiver (SPIRE) instruments, are presented, and the data are analyzed. In Section 3 we present new radiometric properties derived from our thermophysical model (TPM). In Section 4 we feed in our radiometric properties to derive upper limits for the water production rate of both asteroids. In Section 5, we calculate the fraction of ice

coverage required to achieve this upper limit, discuss our results, and present our conclusions.

2. Observations and Data Analysis

2.1. Herschel HIFI Observations

Themis was observed with HIFI on Herschel on 2012 January 30 (see Table 1). The asteroid was traveling inbound (2.92 au) and close to perihelion (2.75 au) when the observation was carried out. Cybele was observed with HIFI on 2012 December 21 (see Table 1) when the asteroid was 3.52 au from the Sun and inbound, having already passed aphelion (3.8 au). It is important to highlight that with the low escape velocity from these asteroids, any escaping water vapor would have been visible to Herschel independent of its source location, as the footprint of the telescope was much larger than the asteroids themselves.

The line emission from the fundamental ortho-H₂O 1₁₀-1₀₁ line at 556.936 GHz was searched for in the lower sideband of the HIFI band 1b mixer. The observations were performed in the frequency-switching observing mode using both the wide-band spectrometer (WBS) and the high-resolution spectrometer (HRS). The spectral resolution of the WBS is 1 MHz (0.54 km s⁻¹ at the frequency of the observed line), while the HRS was used in its high-resolution mode with a resolution of 120 kHz (0.065 km s⁻¹). Initial processing of the HIFI data set was carried out using the standard HIFI processing pipeline of the Herschel Interactive Processing Environment v15.0.1 (HIPE; Ott 2010), followed by processing with the GILDAS CLASS software.

In CLASS, vertical and horizontal polarizations were folded and averaged. The frequency-switching observing mode introduces quite a strong baseline ripple, which was removed through a polynomial baseline correction performed on the final spectra. The averaged and baseline-corrected HRS spectra of the two asteroids are shown in Figures 1(a) and (b). The pointing offset of both the vertical and the horizontal polarization spectra is 3''/5 in band 1b with respect to the target position. The half-power beam width is 38''/1 at 557 GHz. The main beam brightness temperature scale was computed using a forward efficiency of 0.96 and a beam

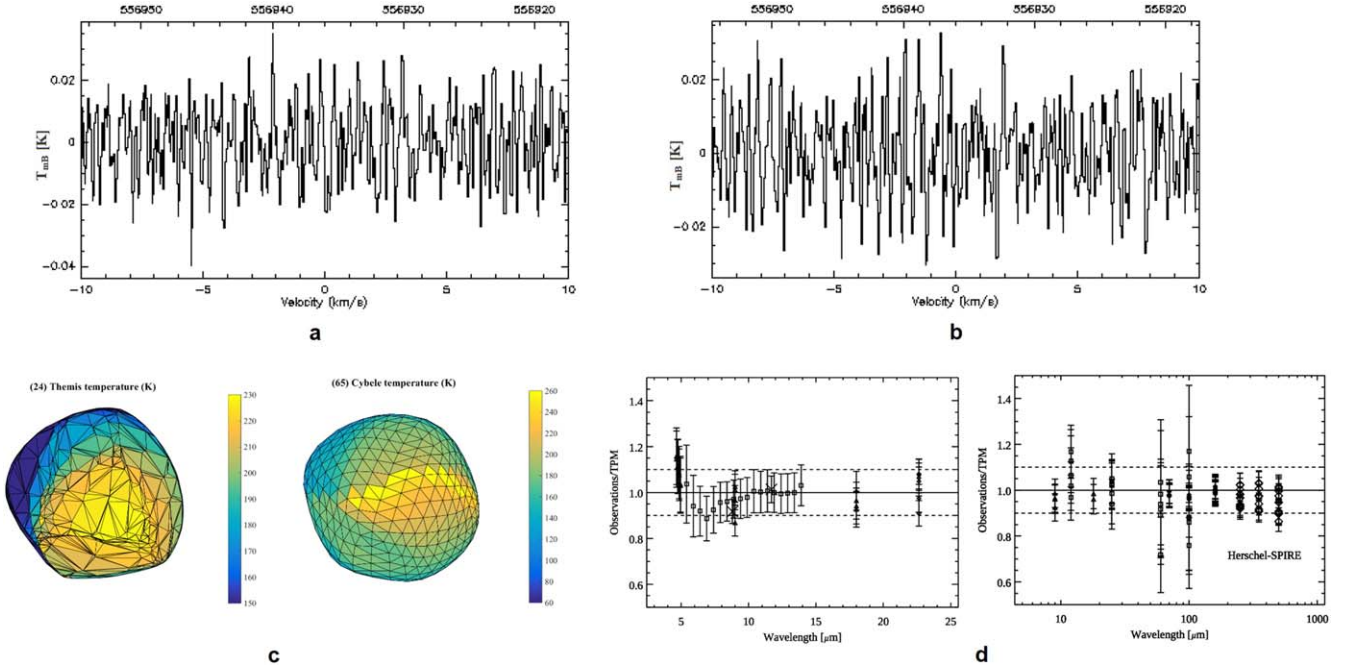


Figure 1. Averaged HIFI spectra and thermophysical modeling output. Shown are the HRS-averaged spectra for (a) asteroid Themis and (b) asteroid Cybele with TPM outputs (c) for Themis (left) and Cybele (right). These outputs represent the Herschel view with orientation “ecliptic sky” at the specific HIFI observing start epochs. The plots in panel (d) show the observations divided by the TPM predictions using the best solution described in the text as a function of wavelength for Themis (left) and Cybele (right). For Themis, the data shown are the good photometric data points coming from Spitzer-IRS (squares), Subaru (crosses), Akari below 5 and above 18 μm (triangles), and WISE-W4 at 22 μm (diamonds). For Cybele, the data are IRAS (squares); AKARI (triangles); ISOCAM (crosses); and PACS, SPIRE, and Spitzer-IRS (diamonds), with identification linked to wavelength.

Table 2
Output Results Following Processing of the Data in Table 1

Target	Herschel/HIFI		Subaru/COMICS			Herschel/SPIRE					
	Line Area 1σ mK km s $^{-1}$ (HRS)	Line Area 1σ mK km s $^{-1}$ (WBS)	Airmass	Flux (Jy)	Err. (Jy)	PSW Flux (Jy)	PSW Err. (Jy)	PMW Flux (Jy)	PMW Err.(Jy)	PLW Flux (Jy)	PLW Err. (Jy)
Themis	2.98	2.82	1.27	3.81	0.22						
			1.26	11.50	0.66						
Cybele	2.96	2.68		n/a		1.680	0.092	0.896	0.049	0.450	0.025
						1.181	0.065	0.630	0.035	0.307	0.017
						0.993	0.055	0.528	0.029	0.260	0.015
						0.857	0.047	0.459	0.025	0.229	0.013
						0.937	0.052	0.493	0.027	0.246	0.014
						1.040	0.057	0.546	0.030	0.271	0.015
						0.795	0.044	0.411	0.023	0.201	0.012
						1.673	0.092	0.883	0.049	0.431	0.024
						1.669	0.092	0.874	0.048	0.431	0.024

Note. Columns: target (the two asteroids), Herschel/HIFI (the calculated line areas for the HRS and WBS spectra for both asteroids), Subaru/COMICS instrument (the airmass, flux, and error obtained for Themis), Herschel/SPIRE instrument (the fluxes and errors derived from the SPIRE 250/350/500 μm observations of Cybele).

efficiency of 0.62. The output line area rms values are provided in Table 2.

Although the H_2O line is not detected in the resultant spectra for either of the two asteroids, sensitive upper limits could be derived. Table 2 provides a summary of the $1\sigma \int TmBdv$ line area upper limits calculated for both asteroids. The 1σ upper limits were computed on a $[-1, 1 \text{ km s}^{-1}]$ window. The mean of the HRS- and WBS-derived values has been used to derive the 3σ upper limits of $8.7 \text{ mK km s}^{-1} \int TmBdv$ for Themis and $8.5 \text{ mK km s}^{-1} \int TmBdv$ for Cybele.

2.2. Observations Used for the Radiometric Analysis

2.2.1. Database of Existing Observations

For the radiometric analysis of these two asteroids, we used a wide range of thermal IR and submillimeter/millimeter measurements. Contrary to Cybele, Themis has not been well observed at thermal IR wavelengths. Besides using a Spitzer-IRS spectrum (Landsman et al. 2016), our study was limited to AKARI and Wide-field Infrared Survey Explorer (WISE) measurements. We used two different AKARI data sets. The

first was taken from the SBNF public database⁹ (Szakáts et al. 2020) and originated from the IRC instrument using the MIR-S (5.8–14.1 μm) and MIR-L (12.4–26.6 μm) cameras. For the second, produced by the IRC-NIR camera, we used the spectral data in the range 4.5–5.0 μm only (Usui et al. 2019), where the fluxes are pure thermal emission. We note that in the case of the WISE data, the W3 data (11.10 μm) were strongly saturated and the saturation-corrected fluxes were problematic, while the W4 (22.64 μm) data were only partly saturated and the saturation-corrected fluxes were of good quality. We added to these observational data sets the Subaru/COMICS data set as presented in Section 2.2.2.

In the case of Cybele, there exists a significant set of observational data available for our radiometric study. In particular, we used Herschel-PACS data (Alf-Lagoa et al. 2020); IRAS (Tedesco & Desert 2002) and AKARI measurements (Usui et al. 2011), both extracted from the SBNF public database (Szakáts et al. 2020); UKIRT-MAX and Infrared Space Observatory (ISO)-ISOPHOT data (Müller & Lagerros 1998, 2002); AKARI data (Usui et al. 2019); multiple ground-based data from the literature and archives, as well as additional spectroscopic and photometric data from ISO-ISOPHOT and ISO-ISOCAM (Müller & Blommaert 2004a); and, finally, Spitzer-IRS data (Licandro et al. 2011). We added to this the Herschel SPIRE as explained in Section 2.2.3.

2.2.2. Subaru/COMICS Data Sets for Themis

The mid-infrared photometric observations for Themis were conducted using COMICS (Kataza et al. 2000), installed at the *f*/12 Cassegrain focus of the 8.2 m Subaru Telescope. The 320×240 pixel Si:As BIB detector for COMICS has 50 μm square pixels, giving a $42'' \times 32''$ field of view with a pixel scale of $0''.135$. The *N*-band filters were centered on 8.8, 11.7, and 12.4 μm with effective bandwidths of 0.8, 1.0, and 1.2 μm , respectively. See Table 1.

To reduce the atmospheric and telescopic background radiation, a standard chopping and nodding method was used. Because it was positioned near Themis in the sky, HD 108985 was selected as an absolute calibration star (Cohen et al. 1999). The fluxes of Themis and HD 108985 as provided in Table 2 were measured through circular apertures with a diameter of more than four times that of the FWHM size using the APPHOT function in the IRAF software. Since the color differences between the spectral energy distributions of Themis and HD 108985 in the N88 and 11.7 filters were found to be about a few percent, color corrections for observations with COMICS were not performed.

2.2.3. SPIRE Data Sets for Cybele

The Herschel SPIRE instrument covering three far-infrared bands—250, 350, and 500 μm —observed Cybele nine times during the period 2009–2012. See Table 1. The observations were taken directly from the Herschel Science Archive.¹⁰ Photometry was carried out using the timeline fitter method available in HIPE. The derived total monochromatic flux densities were color-corrected to account for the assumed spectral index of $\alpha = 2$. A flux calibration uncertainty of 5.5% was added in quadrature for the total error budget. The output

fluxes corresponding to the three SPIRE wavelength bands and associated errors are provided in Table 2.

3. Thermophysical Modeling of the Two Asteroids

A TPM (Lagerros 1996, 1998; Müller & Lagerros 1998, 2002) was used to derive the radiometric properties of the two asteroids. This model has been successfully used in the study of near-Earth asteroids (Müller et al. 2004b, 2011, 2012), main-belt asteroids (Müller & Blommaert 2004a; O'Rourke et al. 2012), and more distant objects (Lim et al. 2010; Müller et al. 2019).

For both asteroids, we performed a radiometric analysis combining all available mid-to-far-IR measurements with the Subaru/COMICS and Herschel/SPIRE values, as described in Section 2.2 of this paper and presented in Tables 1 and 2.

For our work, we followed a similar strategy as in Alf-Lagoa et al. (2020, and references therein). In the case of Themis, nonconvex spin–shape solutions (Viikinkoski et al. 2017; based on two spin solutions from Hanuš et al. 2016), as well as two simpler convex solutions (DAMIT database), were tested against the available thermal measurements presented in Section 2.2 in our model. Since the data coverage in rotational phase, phase angle, aspect angle, and wavelength was very limited, it was not possible to identify the object's true spin and shape properties via our χ^2 approach.

We obtained a best fit, however, using the second convex spin–shape solution with $(\lambda_{\text{ecl}}, \beta_{\text{ecl}}) = (137^\circ, 59^\circ)$ and $P_{\text{sid}} = 8.374187$ hr. This model has 2040 surface elements and 1022 vertices¹¹ (model ID1006; Hanuš et al. 2016). Our resulting derived radiometric properties are thermal inertia $\Gamma = 20^{+25}_{-10}$ $\text{J m}^{-2} \text{s}^{-1/2} \text{K}^{-1}$, effective diameter $D_{\text{eff}} = \text{diameter } 192^{+10}_{-7}$ km, and geometric *V*-band albedo $p_V = 0.07 \pm 0.01$ (connected to an absolute *V*-band magnitude of $H = 7.11$ mag from Oszkiewicz et al. 2011), for an intermediate-to-low level of surface roughness ($0.1 < \text{rms} < 0.5$; Table 4). See Figures 1(c) (left) and (d) (left) for the Themis TPM output. While this multi-observatory data set output provides a diameter consistent with previously published values, it is lower than the NEATM-derived measurements based on Spitzer of 218 ± 1 km (Hargrove et al. 2015).

For Cybele, Viikinkoski et al. (2017) were able to eliminate the pole ambiguity via multiple AO images using a nonconvex shape model with a spin pole at $(\lambda_{\text{ecl}}, \beta_{\text{ecl}}) = (208 \pm 1^\circ, -3 \pm 3^\circ)$ and $P_{\text{sid}} = 6.081435$ hr. They estimated a diameter of 296 ± 25 km, which is within 1σ of the earlier published radiometric diameter of 273 ± 11 km (Müller & Blommaert 2004a) and that published by Alf-Lagoa et al. (2020).

Alf-Lagoa et al. (2020) analyzed IRAS, AKARI, and Herschel-PACS measurements using the latest spin–shape solution (the ADAM model by Viikinkoski et al. 2017) with a spin pole at $(\lambda_{\text{ecl}}, \beta_{\text{ecl}}) = 208^\circ \pm 1^\circ, -3^\circ \pm 3^\circ$ and a rotation period of 6.08 hr. They found that a best-fitting radiometric diameter of 277^{+4}_{-2} km and thermal inertia value of 30^{+10}_{-15} $\text{J m}^{-2} \text{s}^{-1/2} \text{K}^{-1}$ could explain these thermal fluxes very well based on a reduced χ^2 minimum < 1 . Therefore, as in the case of Themis, we used the shape model with the size as a free parameter.

In our work, we used the same nonconvex shape model of Cybele as in Alf-Lagoa et al. (2020), which has 2040 surface elements and 1022 vertices¹² (DAMIT Database ID1843) with

⁹ <https://ird.konkoly.hu/>

¹⁰ The Herschel Science Archive website is https://herschel.esac.esa.int/Science_Archive.shtml.

¹¹ https://astro.troja.mff.cuni.cz/projects/damit/asteroid_models/view/1006

¹² https://astro.troja.mff.cuni.cz/projects/damit/asteroid_models/view/783

a spin pole at $(\lambda_{\text{ecl}}, \beta_{\text{ecl}}) = (207, -6)$ and $P_{\text{sid}} = 6.081435$ hr. The reduced χ^2 minimum was at 0.75 for an intermediate surface roughness (rms of surface slopes of 0.4). We find an effective diameter $D_{\text{eff}} = 282 \pm 9$ km, a best-fit thermal inertia of $\Gamma = 25^{+28}_{-19} \text{ J m}^{-2} \text{ s}^{-1/2} \text{ K}^{-1}$, and a geometric V -band albedo of $p_V = 0.042 \pm 0.005$ (connected to an absolute V -band magnitude of $H = 6.82$ mag from Oszkiewicz et al. 2011; Table 4). Our solution was found to match all photometric IR data points, as well as the Spitzer-IRS spectrum and the ISO-ISOCAM CVF spectrum (except in the range of the emission feature discussed in Müller & Blommaert 2004a). See Figures 1(c) (right) and (d) (right) for the resultant TPM output. The inclusion of the SPIRE data contributed to confirm that Cybele shows a normal submillimeter (spectral) emissivity behavior similar to many other large regolith-covered main-belt asteroids like Ceres, Pallas, and Juno (Müller & Lagerros 1998).

4. Outgassing Rate Upper Limits

To derive the upper limits on the water production rate for the two asteroids, we used a molecular excitation model that calculates the population of the rotational levels of water as a function of distance from the asteroid. Our excitation model takes into account collisions of water and electrons, and infrared pumping of the vibrational bands and treats self-absorption using the escape probability formalism (Zakharov et al. 2007; Biver et al. 2012, 2015). Further to this, the model takes into account the thermal background emission from the asteroid and nonconstant gas kinetic temperature radial profiles (Biver et al. 2019).

Input parameters to the model include the asteroid radius (from our TPM), electron density, gas expansion velocity, derived surface temperature (from our TPM, which includes surface roughness effects that enhance the temperatures significantly), and gas temperature. Synthetic spectra are computed taking into account the transfer of line radiation of ortho-water in the asteroidal “atmosphere.” Since the electron density is not well constrained, a scaling factor of $x_{\text{ne}} = 0.2$ with respect to the standard profile derived from observations of comet 1P/Halley has been used (Hartogh et al. 2010). For the radial gas density profile, we adopted the standard Haser law (Haser 1957). We assumed a nominal expansion velocity v_{exp} of 0.5 km s^{-1} (characteristic of weak comets).

Assuming a rarefied free-expanding exosphere for the asteroids and based on these “nominal” x_{ne} and v_{exp} values, we calculated the water production rates (see Table 3) based on gas kinetic temperature values of 10, 20, and 50 K, as well as a set of variable temperature profiles. We included 50 K because temperatures of approximately 50–60 K are expected for Ceres at 3000 km from its body center (Küppers et al. 2014). We obtained similar results for the two asteroids, irrespective of the temperature profile applied. This suggests that we are more likely sensitive to the gas temperature at some distance from the surface where collisions become too weak.

We find that for the low production rates we estimate, water excitation is not affected significantly by electron collisions because of low electron densities. Applying a value of $x_{\text{ne}} = 0.2$ or 0.0 does not change our results. Using $x_{\text{ne}} = 1.0$ decreases the upper limits on the water production rate by 10%, and doubling the collision rate with neutrals decreases the values by 8%.

Taking into account the above findings, we added a column in Table 3 defining highly conservative 3σ upper limits for the water production rate of $Q(\text{H}_2\text{O}) < 4.1 \times 10^{26}$ molecules s^{-1} for Themis and $Q(\text{H}_2\text{O}) < 7.6 \times 10^{26}$ molecules s^{-1} for Cybele. These values were obtained by assuming a kinetic temperature of 10 K, a high expansion velocity v_{exp} of 0.7 km s^{-1} , and no excitation by photoelectrons, i.e., $x_{\text{ne}} = 0.0$. These upper limits provide more than an order of magnitude improvement on previously published $Q(\text{H}_2\text{O})$ values, which are presented in the final column of Table 3 for comparison purposes. We also derived sensitive 3σ upper limits for the column density of $N_{\text{col}} < 0.58 \times 10^{12} \text{ cm}^{-2}$ for Themis and $N_{\text{col}} < 0.82 \times 10^{12} \text{ cm}^{-2}$ for Cybele (Tables 3 and 4).

5. Discussion and Conclusions

Using a sublimation model, we use the upper limits for the water-loss rate presented in Section 4 to produce equivalent upper limits for the percentage of exposed ice that is present on the surface of the two asteroids. In our analysis, we study the implications of mixing the ubiquitous dark dust and the ice present on the asteroid surfaces at both a fine scale (intimate mixing) and a more macroscopic level (areal mixing), whereby the level of mixing can affect the contribution of the ice albedo to the area-averaged albedo. For intimate mixing, laboratory experiments show that only a few weight percent of dust is sufficient to reduce the albedo of the ice well below 10% (Pommerol et al. 2015). In the areal mixing case, the cleaner the ice is (less mixed with the dust), the brighter (higher Bond albedo) and colder it will be, resulting in less sublimation. This leads to a higher area percentage coverage deduced from the water production rate for the areal mixing case than for the case of intimately mixed ice (Jewitt & Guilbert-Lepoutre 2012).

We used a sublimation model¹³ (Cowan & A'Hearn 1979; slow rotator version) where the rotational pole is pointed toward the Sun. This is appropriate for bodies with a small thermal inertia, as is the case (from our TPM) for Themis and Cybele. This sublimation model provides the average water sublimation rate per surface unit, Z , at a given heliocentric distance. The upper limit on the area of exposed ice A_{exp} is obtained by dividing the upper limit on $Q(\text{H}_2\text{O})$ by Z , and the upper limit on the fraction of the surface occupied by ice (f_{ice}) is obtained by dividing A_{exp} by the asteroid surface area ($4\pi r_N^2$, where r_N is the effective radius). In addition to the heliocentric distance, the input parameters of the model include the Bond albedo of the icy material and the infrared emissivity equal to 0.9.

Figure 2 shows the derived upper limits for the ice coverage of the two asteroids. We plot our water production upper limits against the Bond albedo and the percentage ice coverage; acceptable solutions must lie on or below the water production curves, as otherwise, gas production through sublimation would have been large enough for detection by HIFI. In this figure, we study two scenarios for the water ice interaction with the ubiquitous dark dust of the asteroid. In the first scenario, we gradually mix a low geometric albedo (0.02–0.04) surface dust with ice of an increasing Bond albedo value (brightness), resulting in an areal-type mixture. In the second scenario, we study the intimate mixture case on the basis that the Bond albedo of the asteroid represents the combined albedos of the icy dust mixture.

¹³ <https://pdssbn.astro.umd.edu/tools/ma-evap/>

Table 3
H₂O Production Rate ($Q(\text{H}_2\text{O})$) and Column Density (N_{col}) Derived for Different Gas Kinetic Temperatures

		Kinetic Temperature T_{kin} (K)				Variable Temperature T_{var} (K)			Previously Published Data
		Upper Limits	10	20	50	($T_f = 10$)	($T_f = 20$)	($T_f = 50$)	
Themis	$Q(\text{H}_2\text{O})$ (molecules s ⁻¹)	$<4.1 \times 10^{26}$	$<3.12 \times 10^{26}$	$<2.78 \times 10^{26}$	$<2.5 \times 10^{26}$	$<2.63 \times 10^{26}$	$<2.59 \times 10^{26}$	$<2.55 \times 10^{26}$	(i) $< 1.3 \times 10^{28}$, (ii) $< 1.0 \times 10^{28}$, (iii) $< 4.5 \times 10^{27}$
	N_{col} (cm ⁻²)	$<0.58 \times 10^{12}$	$<0.58 \times 10^{12}$	$<0.52 \times 10^{12}$	$<0.47 \times 10^{12}$	$<0.49 \times 10^{12}$	$<0.49 \times 10^{12}$	$<0.48 \times 10^{12}$	
Cybele	$Q(\text{H}_2\text{O})$ (molecules s ⁻¹)	$<7.6 \times 10^{26}$	$<5.76 \times 10^{26}$	$<5.04 \times 10^{26}$	$<4.46 \times 10^{26}$	$<4.71 \times 10^{26}$	$<4.63 \times 10^{26}$	$<4.53 \times 10^{26}$	(i) $< 1.2 \times 10^{28}$
	N_{col} (cm ⁻²)	$<0.82 \times 10^{12}$	$<0.84 \times 10^{12}$	$<0.73 \times 10^{12}$	$<0.65 \times 10^{12}$	$<0.69 \times 10^{12}$	$<0.67 \times 10^{12}$	$<0.66 \times 10^{12}$	

Note. The temperatures are either constant throughout the coma (T_{kin}) or variable ($T_{\text{var}} = (T_0 - T_f) r_N / r + T_f$), with $T_0 = 155$ K for Themis and $T_0 = 138$ K for Cybele, corresponding to 86% of the surface temperature (Crifo et al. 2002); r_N is the radius of the asteroid derived from our TPM, and r is the distance to the body center. The ‘‘Upper Limits’’ column corresponds to the worst-case estimate of the upper limit, whereby $T_{\text{kin}} = 10$ K, $v_{\text{exp}} = 0.7$, and $x_{\text{ne}} = 0$ (see text). All other estimates are performed with the optimal values $v_{\text{exp}} = 0.5$ and $x_{\text{ne}} = 0.2$. Previously published data references are as follows: (i) Jewitt & Guilbert-Lepoutre (2012); (ii) Lovell et al. (2010); and (iii) McKay et al. (2017).

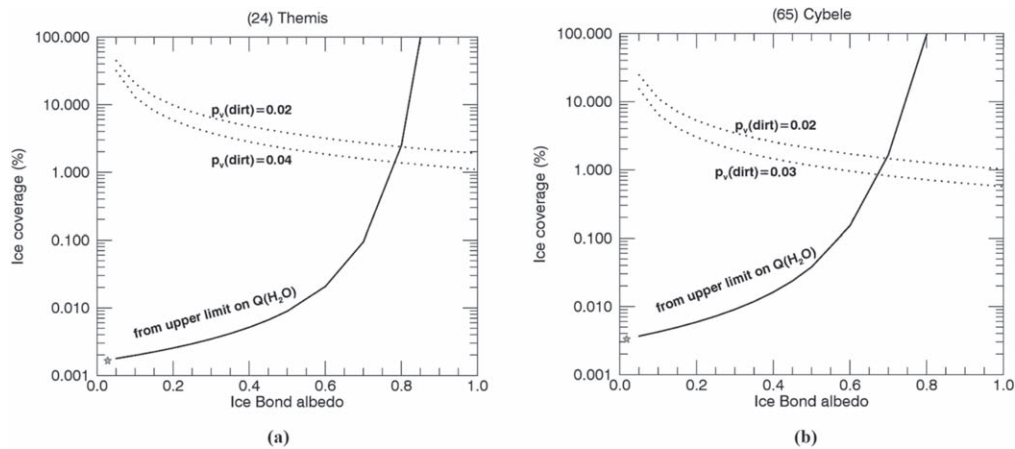


Figure 2. Derived allowed values for the ice coverage for (a) Themis and (b) Cybele as a function of the Bond albedo of surface ice. The solid curve represents the $Q(\text{H}_2\text{O})$ constraint derived for each asteroid. Acceptable solutions must lie on or below this curve, as otherwise, gas production through sublimation would have been large enough for detection by HIFI. The dotted curves reflect the albedo constraint (see text) for geometric albedos of surface dust only $p_v(\text{dust})$ in the range 0.02–0.04 for Themis and 0.02–0.03 for Cybele. Acceptable solutions for the areal mixing case must lie along or between these dotted curves to guarantee the area-averaged albedo matches our modeled TPM value. The purple stars represent the positions of the corresponding intimate mixing results.

Table 4
Summary of Main Results of This Paper

Target	$Q(\text{H}_2\text{O})$ (molecules s^{-1})	N_{col} (cm^{-2})	Intimate f_{ice} (%)	Areal f_{ice} (%)	Γ ($\text{J m}^{-2} \text{s}^{-1/2} \text{K}^{-1}$)	D (km)	p_V (Geometric)	p_V (Bond)
Themis	$<4.1 \times 10^{26}$	$<0.58 \times 10^{12}$	0.0017	1.4–2.2	20^{+25}_{-10}	192^{+10}_{-7}	0.07 ± 0.007	0.027
Cybele	$<7.6 \times 10^{26}$	$<0.82 \times 10^{12}$	0.0033	0.8–1.5	25^{+28}_{-19}	282 ± 9	$0.042^{+0.03}_{-0.02}$	0.019

Note. Here $Q(\text{H}_2\text{O})$ is the water production rate upper limit, N_{col} is the column density upper limit, f_{ice} is the fraction of ice coverage depending on whether it is an intimate or areal mixture, Γ is the thermal inertia, D is the effective diameter, and p_V is the V-band geometric and Bond albedo.

Applying scenario 1 and in line with the approach of Jewitt & Guilbert-Lepoutre (2012), we plot two dotted lines in Figure 2 matching with geometric albedo values for $p_v(\text{dust}) = 0.02$ –0.04 for Themis and 0.02–0.03 for Cybele, corresponding to the least reflective asteroid surfaces known. Due to its already very low albedo (from our TPM) of 0.042, 0.03 is set as a conservative value for the Cybele upper range. The two constraints (water production rate limit and albedo) are found to be acceptably achieved only if the water ice on the two asteroids is very bright (Bond albedo of 0.8 for Themis, 0.7 for Cybele) and the water ice covers $<2.2\%$ of the surface for Themis and $<1.5\%$ for Cybele. Upper limits of 2.2% and 1.5% ice, respectively, on the surface of the Themis and Cybele asteroids will lead to similar upper limits in the depth of water ice in the $3.1 \mu\text{m}$ absorption feature, as pure water ice is fully absorbing at this wavelength (e.g., Protopapa et al. 2014). As the $3.1 \mu\text{m}$ band depth of both asteroids is $\sim 10\%$ of the local continuum (Rivkin & Emery 2010; Licandro et al. 2011), we conclude that for areal mixing, the $3.1 \mu\text{m}$ absorption feature cannot be explained by surface water ice on these asteroids.

In scenario 2, we assume that the water ice is intimately mixed with the dark surface material of the asteroids (as observed on other solar system objects, including 67P) and, as such, corresponds to the area-averaged Bond albedo of the asteroid. A value for the bolometric Bond albedo (A) of 0.027 was calculated for Themis and 0.019 for Cybele based on the formula $A = p * q$, where p is the bolometric geometric albedo assumed to be equal to the V-band albedo p_V and $q = 0.290 + 0.684 * G$. Here G is the slope parameter in the H-G system (Bowell et al. 1989), and it was determined to be 0.16 for Themis and 0.23 for Cybele (Oszkiewicz et al. 2011). From Figure 2 (purple stars) and based on these Bond albedo

values, we obtain upper limits for the fraction of the surface covered by ice to be 0.0017% for Themis and 0.0033% for Cybele, meaning that only a tiny fraction of intimately mixed ice is present on the surface of these asteroids. These values are an order of magnitude lower than those obtained by Jewitt & Guilbert-Lepoutre (2012) and McKay et al. (2017). Like them, we conclude that such an ice–dust mixture percentage is entirely insufficient to explain the $3.1 \mu\text{m}$ absorption.

To appreciate the possible percentage of intimately mixed ice below the surface, we compare it with values obtained from 67P/Churyumov–Gerasimenko. On 67P, the ice was observed to be intimately mixed with the dust, visible in localized regions, and considered to be just below the surface (Fornasier et al. 2016b). We applied the above model using $Q(\text{H}_2\text{O})$ measured values of 67P at 3 au based on a Bond albedo of 0.012 at 3 au (Fornasier et al. 2015) and emissivity of 0.97 (Spohn et al. 2015). We find an ice coverage of 0.6% at 3 au pre-perihelion and 0.2% at 3 au post-perihelion, percentages more than 2 orders of magnitude higher than those derived for the asteroids. In this comparison, if ice is indeed present just below the asteroid’s surface and intimately mixed with dust, as in comets, then there is a very low amount present.








While surface water ice may not be the reason for the $3.1 \mu\text{m}$ absorption feature, the $3 \mu\text{m}$ region is known to host other volatile species that do show similar absorption curves. The ammonium (NH_4^+) ion has a band center near $3.1 \mu\text{m}$ and was interpreted to be present in the (1) Ceres spectrum (King et al. 1992). Poch et al. (2020) recently compared the $3.2 \mu\text{m}$ spectra of ammonium salts found on comet 67P (Altwegg et al. 2020) with the $3.1 \mu\text{m}$ feature on Themis and Cybele, finding a distinct correlation between the two. Similar features have been observed on the Jupiter Trojan asteroids and the small moon

Himalia matching with ammoniated minerals on their surfaces (Brown 2016; Poch et al. 2020) at this wavelength. Further to the above, minerals such as brucite (Beck et al. 2011), magnetite (Yang & Jewitt 2010), and adsorbed water molecules in lunar regolith (Clark 2009) all represent other possible alternative explanations to the presence of surface water ice.

In conclusion, we present highly conservative, sensitive 3σ upper limits for the water production rate on (24) Themis and (65) Cybele. Using these limits to model the maximum surface ice fraction, we find that the $3.1\ \mu\text{m}$ absorption feature cannot be explained by water ice, be it areal or intimately mixed. Recognizing the numerous spacecraft that have visited asteroids and comets where far too little surface ice has been detected to be visible in disk-integrated spectra, our results serve to confirm the continued difficulty in observing ice from the Earth, whether via ground- or space-based observatories.

This study was based in part on data collected using the Subaru Telescope, which is operated by NAOJ. S.H. and H.F. would like to acknowledge H. Kataza, T. Ootsubo, T. Sekiguchi, and I. Yamamura for their helpful comments and discussions. The work of S.H. was supported by the Hypervelocity Impact Facility, ISAS, JAXA. T.M. has received funding from the European Union's Horizon 2020 Research and Innovation Programme under grant Agreement No. 687378 as part of the project "Small Bodies Near and Far" (SBNF). We acknowledge the use of the GILDAS CLASS software (<http://www.iram.fr/IRAMFR/GILDAS>) in the processing of the HIFI data. We would like to thank the anonymous referee for the insightful and helpful comments provided.

ORCID iDs

L. O'Rourke  <https://orcid.org/0000-0002-8507-3772>
 T. G. Müller  <https://orcid.org/0000-0002-0717-0462>
 D. Bockelée-Morvan  <https://orcid.org/0000-0002-8130-0974>
 S. Hasegawa  <https://orcid.org/0000-0001-6366-2608>
 I. Valtchanov  <https://orcid.org/0000-0001-9930-7886>
 M. Küppers  <https://orcid.org/0000-0002-5666-8582>
 S. Fornasier  <https://orcid.org/0000-0001-7678-3310>
 H. Fujiwara  <https://orcid.org/0000-0001-6536-8656>

References

Alí-Lagoa, V., Müller, T. G., Kiss, C., et al. 2020, *A&A*, 638, A84
 Altwegg, K., Balsiger, H., Hänni, N., et al. 2020, *NatAs*, 4, 533
 Beck, P., Quirico, E., & Sevestre, D. 2011, *A&A*, 526, A85
 Biver, N., Bockelée-Morvan, D., Hofstadter, M., et al. 2019, *A&A*, 630, A19
 Biver, N., Bockelée-Morvan, D., Morena, R., et al. 2015, *SciA*, 1, e1500863
 Biver, N., Crovisier, J., Bockelée-Morvan, D., et al. 2012, *A&A*, 539, A68
 Bockelée-Morvan, D., Biver, N., Crovisier, J., et al. 2010, *BAAS*, 42, 946
 Bowell, E. G., Hapke, B., & Domingue, D. 1989, in *Asteroids II*, ed. R. P. Binzel, T. Gehrels, & M. S. Matthews (Tucson, AZ: Univ. of Arizona Press), 524

Brown, M. E. 2016, *AJ*, 152, 159
 Campins, H., Hargrove, K., Pinilla-Alonso, N., et al. 2010, *Natur*, 464, 1320
 Clark, R. N. 2009, *Sci*, 326, 562
 Cohen, M., Walker, R. G., Carter, B., et al. 1999, *AJ*, 117, 1864
 Combe, J. Ph., McCord, T. B., Tosi, F., et al. 2016, *LPSC*, 47, 1820
 Cowan, J. J., & A'Hearn, M. F. 1979, *M&P*, 21, 155
 Crifo, J. F., Loukianov, G. A., Rodionov, A. V., et al. 2002, *Icar*, 156, 249
 de Graauw, T., Helmich, F. P., Phillips, T. G., et al. 2010, *A&A*, 518, L6
 Fornasier, S., Hasselmann, P. H., Barucci, M. A., et al. 2015, *A&A*, 583, A30
 Fornasier, S., Lantz, C., Barucci, M. A., et al. 2014, *Icar*, 233, 163
 Fornasier, S., Lantz, C., Perna, D., et al. 2016a, *Icar*, 269, 1
 Fornasier, S., Lazzarin, M., Barbieri, C., et al. 1999, *A&AS*, 135, 65
 Fornasier, S., Mottola, S., Keller, H., et al. 2016b, *Sci*, 54, 1566
 Hanuš, J., Durech, J., Oszkiewicz, D. A., et al. 2016, *A&A*, 586, A108
 Hargrove, K. D., Emery, J. P., Campins, H., et al. 2015, *Icar*, 254, 150
 Hargrove, K. D., Kelley, M. S., Campins, H., et al. 2012, *Icar*, 221, 453
 Hartogh, P., Crovisier, J., de Val-Borro, M., et al. 2010, *A&A*, 518, L150
 Haser, L. 1957, *Liege Inst. Astrophys. Rep.*, 394
 Hsieh, H. H., & Jewitt, D. 2006, *Sci*, 312, 561
 Jewitt, D., & Guilbert-Lepoutre, A. 2012, *AJ*, 143, 21
 Kataza, H., Okamoto, Y., Takubo, S., et al. 2000, *Proc. SPIE*, 4008, 1144
 King, T. V. V., Clark, R. N., Calvin, W. M., et al. 1992, *Sci*, 255, 1551
 Küppers, M., O'Rourke, L., Bockelée-Morvan, D., et al. 2014, *Natur*, 505, 525
 Lagerros, J. S. V. 1996, *A&A*, 310, 1011
 Lagerros, J. S. V. 1998, *A&A*, 332, 1123
 Landsman, Z., Licandro, J., Campins, H., et al. 2016, *Icar*, 269, 62
 Licandro, J., Campins, H., Kelley, M., et al. 2011, *A&A*, 525, A34
 Lim, T. L., Stansberry, J., Müller, T. G., et al. 2010, *A&A*, 518, 148
 Lovell, A. J., Fernandez, Y. R., Campins, H., et al. 2010, *BAAS*, 42, 1036
 McKay, A. J., Bodewits, D., & Jian-Yang, L. 2017, *Icar*, 286, 308
 McKay, A. J., Chanover, N. J., di Santi, M. A., et al. 2014, *Icar*, 231, 193
 McKay, A. J., Cochran, A., Disanti, M. A., et al. 2015, *Icar*, 250, 504
 Müller, T. G., & Blommaert, J. A. D. L. 2004a, *A&A*, 418, 347
 Müller, T. G., Durech, J., Hasegawa, S., et al. 2011, *A&A*, 525, 145
 Müller, T. G., Kiss, C., Ali-Lagoa, V., et al. 2019, *Icar*, 334, 39
 Müller, T. G., & Lagerros, J. S. V. 1998, *A&A*, 338, 340
 Müller, T. G., & Lagerros, J. S. V. 2002, *A&A*, 381, 324
 Müller, T. G., O'Rourke, L., Barucci, A. M., et al. 2012, *A&A*, 548, 36
 Müller, T. G., Sterzik, M. F., Schütz, O., et al. 2004b, *A&A*, 424, 1075
 Nesvorný, D. 2012, *Nesvorný HCM Asteroid Families V2.0, EAR-A-VARGBDET-5-NESVORNYFAM-V2.0, NASA Planetary Data System*
 O'Rourke, L., Müller, T. G., Valtchanov, I., et al. 2012, *P&SS*, 55, 192
 O'Rourke, L., Snodgrass, C., de Val Borro, M., et al. 2013, *ApJL*, 774, L13
 Oszkiewicz, D. A., Muinonen, K., Bowell, E., et al. 2011, *JQSRT*, 112, 1919
 Ott, S. 2010, in *ASP Conf. Ser. 434, Astronomical Data Analysis Software and Systems XIX*, ed. Y. Mizumoto, K.-I. Morita, & M. Ohishi (San Francisco, CA: ASP), 139
 Pilbratt, G. L., Riedinger, J. R., Passvogel, T., et al. 2010, *A&A*, 518, L1
 Poch, O., Istiqomah, I., Quirico, E., et al. 2020, *Sci*, 367, 7462
 Pommerol, A., Thomas, N., El-Maary, M. R., et al. 2015, *A&A*, 583, A25
 Protopapa, S., sunshine, J., Feaga, L. M., et al. 2014, *Icar*, 238, 191
 Rivkin, A. S., & Emery, J. P. 2010, *Natur*, 464, 1322
 Rivkin, A. S., Howell, E. S., Vilas, F., et al. 2002, in *Asteroids III*, ed. W. F. Bottke, Jr. et al. (Tucson, AZ: Univ. Arizona Press), 235
 Spohn, T., Knollenberg, J., Ball, A. J., et al. 2015, *Sci*, 349, 6247
 Szakáts, R., Müller, T. G., Alí-Lagoa, V., et al. 2020, *A&A*, 635, A54
 Takir, D., & Emery, J. P. 2012, *Icar*, 219, 641
 Tedesco, E. E., & Desert, F.-X. 2002, *AJ*, 123, 1056
 Usui, F., Hasegawa, S., Ootsubo, T., et al. 2019, *PASJ*, 71, 1
 Usui, F., Kuroda, D., Müller, T. G., et al. 2011, *PASJ*, 63, 1117
 Viikinkoski, M., Hanuš, J., Kaasalainen, M., et al. 2017, *A&A*, 607, A117
 Yang, B., & Jewitt, D. 2010, *AJ*, 140, 692
 Zakharov, V., Bockelée-Morvan, D., Biver, N., et al. 2007, *A&A*, 473, 303